Chapter 11

Extension of the Wavelength Regime

The direct bandgap of Ge at 0.8 eV restricts the available wavelength regime in Ge/Si-based photonics from λ = 1.2 μm (Si absorption) to 1.55 μm (Ge bandgap). Some minor modification allows the Ge direct bandgap to be extended to 1.65 μm, covering both most important telecommunication wavelengths, around 1.3 μm and around 1.55 μm. The minor modification includes thermal mismatch strain (tensile strain of ε = 0.2% [1]) and bandgap narrowing from high doping levels [2].

Substantial increase of the upper wavelength limit to beyond 2 μm needs either intraband transition from multiquantum wells (MQWs) [3] or interband transitions from heavily strained Ge [4] or from GeSn alloys [5]. Heavily strained Ge is limited in thickness (at a critical thickness the strain of lattice mismatched layers relaxes [6]). So, GeSn arises as the preferred material to shift the bandgap to lower values than 0.8 eV, which means to higher wavelengths like 1.55 μm.

11.1 Germanium Tin

The research on germanium tin (GeSn) is further stimulated by the predictions of a direct bandgap semiconductor at rather low Sn amounts (around 10%) by prospects for high-speed electronics

Silicon-Based Photonics
Erich Kasper and Jinzhong Yu

ISBN 978-981-4303-24-8 (Hardcover), 978-1-315-15651-4 (eBook)
www.jennystanford.com

(high carrier mobility) and by challenges from material science (nonequilibrium growth for GeSn alloys with Sn above 1%).

11.1.1 Bandgap of GeSn: Indirect to Direct Transition

A rough estimate of the indirect bandgap E_{gL} (L minimum along 111 is the lowest indirect transition from Ge) and the energy difference $\Delta E_g(L/\Gamma)$ between the L minimum and the direct transition (Γ point) may be obtained by a graph showing these variables as functions of $Z^{1/3}$ (Z is the atomic number).

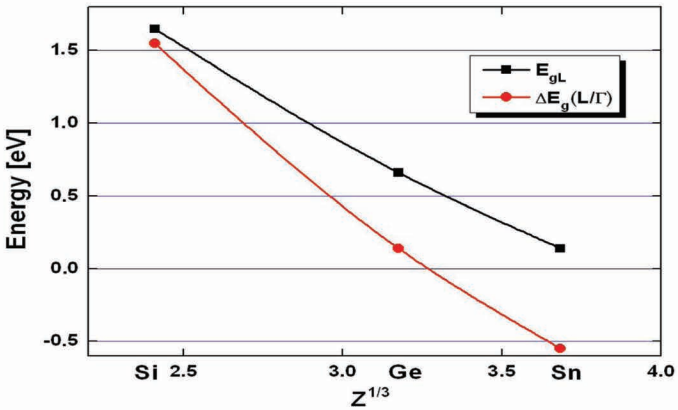

Figure 11.1 Energy values of E_{gL} and $\Delta E_g(L/\Gamma)$ as functions of $Z^{1/3}$.

Both energies show a monotonic behavior with only slight bowing. The $\Delta E_g(L/\tau)$ curve crosses (Fig. 11.1) zero energy (which means direct and indirect transitions have the same energy) at GeSn with rather low Sn amount (about 10%). At higher Sn amounts the semiconductor GeSn is the only bulk group IV semiconductor with a direct bandgap. More sophisticated bandgap theories and optical measurements confirm this predicted transition [7].

The bandgap (Fig. 11.2) as a function of the Sn amount x shows rather strong bowing, with bowing parameters b = 1.94 eV for E_{gdir} and b = 1.23 eV for E_{gL}.

$$E_g(x) = (1 - x)E_g(\text{Ge}) + x \cdot E_g(\text{Sn}) - bx(1 - x) \qquad (11.1)$$

The indirect to direct crossover is predicted at x = 0.11 and E_g = 0.477 eV by this theory. Later Alberi et al. [8] improved the calculation and she could explain the strong bowing behavior.

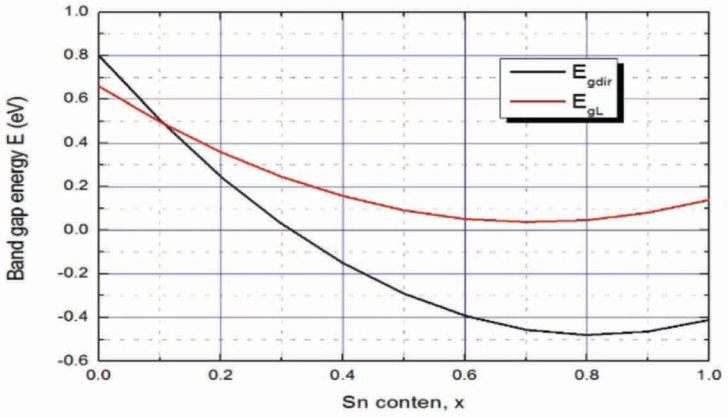

Figure 11.2 Direct E_{gdir} and indirect E_{gL} bandgap of GeSn as functions of Sn amount using data from Ref. [7].

The composition dependence of an alloy's bandgap can be estimated to the first degree by the linear interpolation between the values of the endpoint materials. This linear interpolation is known as generalized Vegard's law (Vegard [9] used it for lattice constant considerations) or, specifically for band properties, as virtual crystal approximation. Band bowing is typically described in a second approximation by a parabolic relationship. Band bowing is primarily caused by constituent mismatch and disorder-related potential fluctuations. While the b values of the bowing parameters in most alloys are smaller than their bandgaps, such as in the case of SiGe ($b > 0.14$), the bowing parameter for GeSn is around twice the gap energy. The electronic structures of highly mismatched alloys have been understood in terms of a band anticrossing model [8]. From this model also assessments of the bowing of band offsets and of the spin-orbit splitting (Δ_0) in the valence band are made.

Type I band alignment between Ge and α-Sn is assumed with ΔE_C(Ge/Sn) = 1 eV and ΔE_V(Ge/Sn) = 0.2 eV. (Remark: We count positive energy values for type I alignment). The direct conduction band offset ΔE_C(Ge/GeSn) of the alloy/Ge interface is then described by

$$\Delta E_C(x) = 1.0 \text{ eV} \cdot x - b_{CB}x(1-x) \tag{11.2}$$

and

$$\Delta E_V(x) = 0.2 \text{ eV} \cdot x - b_{VB}x(1-x). \tag{11.3}$$

Similarly, the valence band offset $\Delta E_V(x)$ is described by Eq. 11.3.

Alberi et al. [8] calculated b_{CB} = 0.7 eV and b_{VB} = 1.24 eV, which exhibit a larger valence band bowing than earlier assessments [10] of b_{CB} = 1.62 eV and b_{VB} = 0.32 eV. The spin-orbit split-off Δ_0 varies rather linearly between the values of Ge (0.3 eV) and α-Sn (0.8 eV).

$$\Delta_0(x) = 0.3\ \text{eV}(1-x) + 0.8\ \text{eV} \cdot x \tag{11.4}$$

11.1.2 Epitaxial Layer Structures on Silicon

On silicon substrates (bulk Si or silicon on insulator [SOI]) we mainly see the four typical epitaxial configurations as shown in Fig. 11.3.

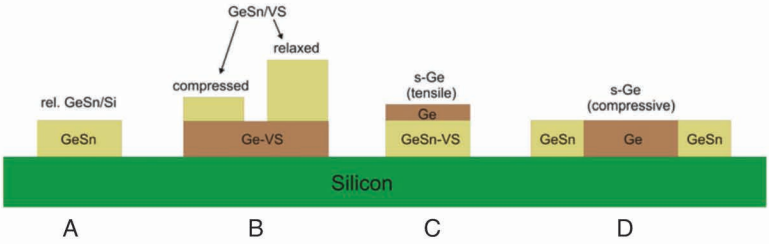

Figure 11.3 Typical GeSn growth structures.

Configuration A shows a straightforward growth of the GeSn layer directly on the Si substrate. The lattice mismatch f is high (linear approximation = 4.3% + 14.7% · x), which results in a strain-relaxed layer already at thicknesses of a few nanometers. In configuration B the GeSn layer is grown on a virtual substrate (Ge VS) composed of a relaxed Ge buffer on Si. The lattice mismatch of low-Sn-content layers relative to the underlying Ge VS is low (f = 14.7% · x), which is comparable with SiGe on Si layers of around 4 × Ge content (e.g., a 5% Sn alloy on a Ge layer is comparable to a 20% Ge alloy on a Si layer). Thin layers are compressively strained, whereas thick layers tend to be strain relaxed. One should consider that the metastable growth regime is large because of the generally low growth temperatures of GeSn alloy layers. For optical properties (direct bandgap) and for electronic properties (high mobility) a tensile strained layer is preferred (configuration C). Here on top of configuration A (relaxed GeSn) a Ge layer or a GeSn layer with lower Sn content is grown (thin enough to be strained). The resulting strain status is a tensile

strain. Configuration D is similar for Ge channel transistors to the now used selective source/drain (S/D) regions in p-type Si channel field-effect transistors. The S/D region is grown by selective epitaxy, and it compresses the Ge channel region if GeSn is used for S/D.

The heterostructure has to be combined with a dopant structure for a device application. Let us discuss this with the example of a light-emitting diode (LED) structure as proposed by Sun et al. [11]. Figure 11.4 gives a schematic scheme of the structure, starting from the bottom with a p-type substrate (SOI) and a p-type relaxed buffer from GeSn.

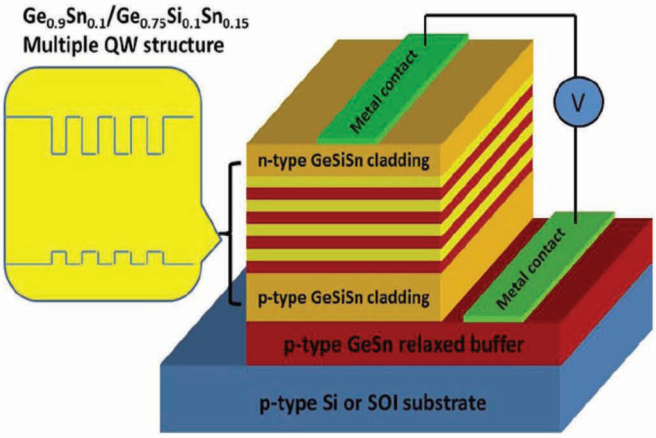

Figure 11.4 Proposal of an LED/laser device structure with active quantum wells from GeSn alloys. Reprinted with permission from Ref. [11] © The Optical Society.

This corresponds to the growth structure A in Fig. 11.3, and it may be described as a virtual GeSn substrate (GeSn VS) as the real substrate is Si but the surface lattice constant is that of GeSn. On this GeSn VS the p-i-n LED follows, which contains a p-type GeSiSn cladding (bottom contact), an intrinsic layer composed of multiple quantum wells (MQWs) from GeSn wells and GeSiSn barriers, and finally an n-type GeSiSn cladding (top contact). The material choice for the claddings and the MQW was such that the strain in the LED was small enough to avoid dislocation generation inside the LED (remember, the GeSn VS contains a misfit dislocation network to allow for lattice accommodation). An equal lattice constant within

the MQW was obtained by a combination of binary GeSn and ternary GeSiSn alloy.

11.1.3 Optical and Electrical Results

The basic doping structure is a p-i-n or p/n junction with a voltage-dependent depletion layer at the junction. In the case of metal-semiconductor-metal device structures the highly doped contact layers are replaced by metal layers, which creates a depletion layer (Schottky contact) in the semiconductor.

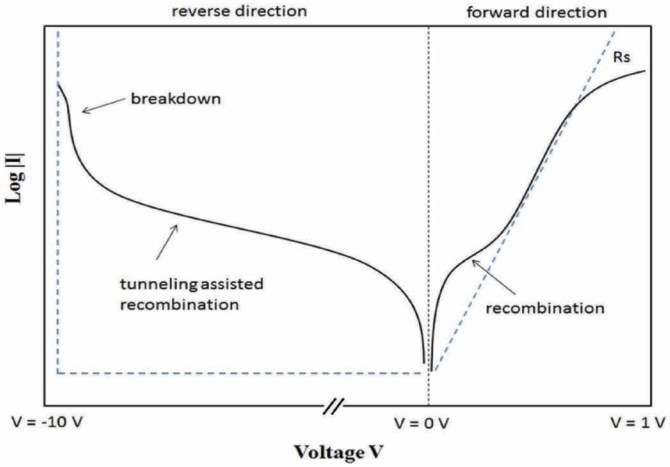

Figure 11.5 Principal scheme of the current characteristics of a junction device in a semilog presentation (log|*I*|vs. *V*). Full line: real device; broken line: ideal device with a low recombination center density.

The electrical characterization is important from a practical viewpoint (choice of operating points, noise, and power consumption) and from a characterization viewpoint (rough estimate of the device material quality). Figure 11.5 shows the principal electrical characteristics of a junction device. Ideally (very high quality, very low recombination center density), the forward characterization follows an exponential increase caused by diffusion currents.

$$\ln I = A + B(\mathrm{q}V/\mathrm{k}T) \tag{11.5}$$

$$B = 0.4343 = \log(e),$$

which means a decade increase of current I at a 60 mV voltage V increase (T = 300 K). The absolute value of the ideal current is proportional $\exp(-E_g/kT)$. The ideal reverse current is low and constant up to the avalanche breakdown voltage. The real forward characteristics are influenced by the series resistance (damping of the exponential increase at high currents), by the recombination of carriers in the depletion layer (increase of current at a low forward voltage), and by tunneling-assisted recombination (reverse voltage).

In devices on a VS usually recombination currents dominate because the dislocations (threading dislocations cross the depletion layer) are very active recombination centers. Carrier recombination from point defects add to the current because the low growth temperature of GeSn alloys (see next section) creates point defect supersaturating. An example [12] is shown in Fig. 11.6, where the reverse current densities of GeSn p-i-n diodes with different Sn contents are compared with a Ge reference diode.

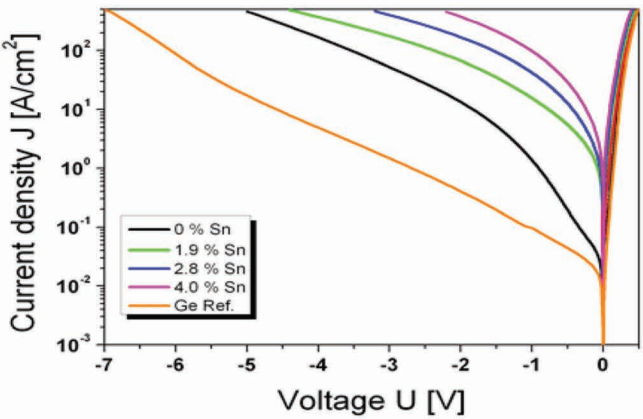

Figure 11.6 Dark current versus voltage for GeSn and Ge photodiodes. Reproduced from Ref. [12], with the permission of AIP Publishing.

The Ge reference diode was grown at 330°C; the tunneling-assisted recombination is mainly caused by the threading dislocations from the Ge VS. The GeSn exhibited higher reverse currents because of the additional point defects generated at the GeSn growth temperature of 100°C. This is easily demonstrated with a Ge p-i-n diode (Sn = 0%) grown at the lower temperature (100°C). The same structure and

dislocation density as the Ge reference but a higher reverse current prove a recombination from dislocation and point defects. Material science research is strongly directed to reduce both contributions.

The lower bandgap of GeSn shifts the absorption edge more into the infrared region [13–15]. In a p-i-n junction, that absorption edge can easily be investigated by the photocurrent [12]. The photocurrent near the absorption edge is linearly dependent on the absorption coefficient α and the thickness t, respectively.

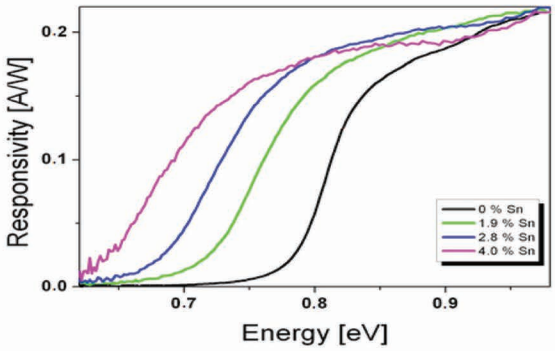

Figure 11.7 Photoresponsivity [12] of GeSn photodiodes with different Sn amounts.

Figure 11.7 demonstrates the infrared shift (lower energy) of the photoresponsivity of GeSn alloys with Sn amounts of a few percent.

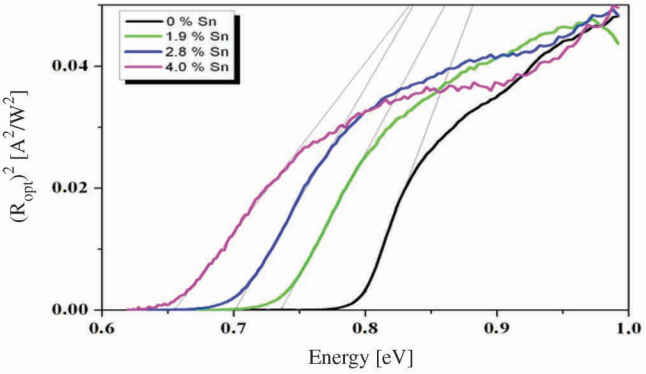

Figure 11.8 Square of the optical responsivity versus energy. A linear increase above the bandgap is typical for direct bandgap transitions. Calculated with data from Fig. 11.7.

The absorption edge is mainly caused by direct transition. Figure 11.8 shows the square of the responsivity, which linearly increases with ($hv - E_g$) as requested for direct transitions.

The dominant photoluminescence (PL) and electroluminescence (EL) lines originated also from direct transitions [16–18]. Figure 11.9 shows a sequence of PL spectra from GeSn alloys with low Sn content (up to 3%). Already small amounts of Sn cause an observable infrared shift of the PL spectra.

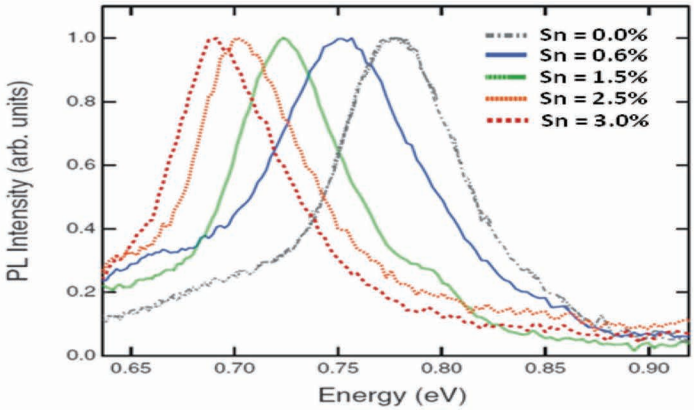

Figure 11.9 Photoluminescence from GeSn on Si. Reproduced from Ref. [17], with the permission of AIP Publishing.

Light emission from GeSn LEDs confirm the redshift of device luminescence [18] with Sn amount. The next figure (Fig. 11.10) compares the emission from a relaxed Ge with that of a compressively strained GeSn (1.3% Sn) LED, both grown on a Ge VS. The GeSn LED shows a direct transition–dominated emission with a clear redshift to a lower emission wavelength. The direct transition dominates in these indirect semiconductors because the direct transition probability is much larger than that of the more populated indirect transition.

A compilation of different methods and authors reveals a rather clear picture for GeSn with low amounts of Sn (up to 7%). The dominant optical absorption and emission process relates to the direct bandgap transition although the semiconductor GeSn is indirect in this low-Sn-content regime. The energy gap decreases (redshift) much more rapidly with Sn content than expected from a

linear interpolation, which indicates a strong bowing of the bandgap. The experimental data from the photocurrent [19], PL [17], EL [20], and photoreflection [21] are compared with the theory [8, 22]. They show acceptable agreement within the uncertainties given by the strain in the devices. The dominance of the direct transition made it difficult to measure the indirect-direct band crossover because the weak indirect transition is hard to measure in the thin epitaxial layers. The bowing parameter b describes the parabolic deviation from a linear interpolation. The values for the bowing parameter for the direct transition in GeSn are around 2.5 eV (2.44 eV in Ref. [21], 2.92 eV in Ref. [23], and 2.88 eV in Ref. [24]).

A careful interpretation of experimental observations [22] delivers 7.1% Sn content in strain-relaxed GeSn as a crossover point between direct and indirect bands.

Recent investigations of GeSn alloys with higher Sn concentrations (15%–30% Sn content) demonstrated a clear shift [24] of the absorption edge into the mid-infrared (8 µm wavelength). There are also hints that the parabolic interpolation of the bandgap energy has to be replaced in this higher Sn content regime by a cubic-order equation.

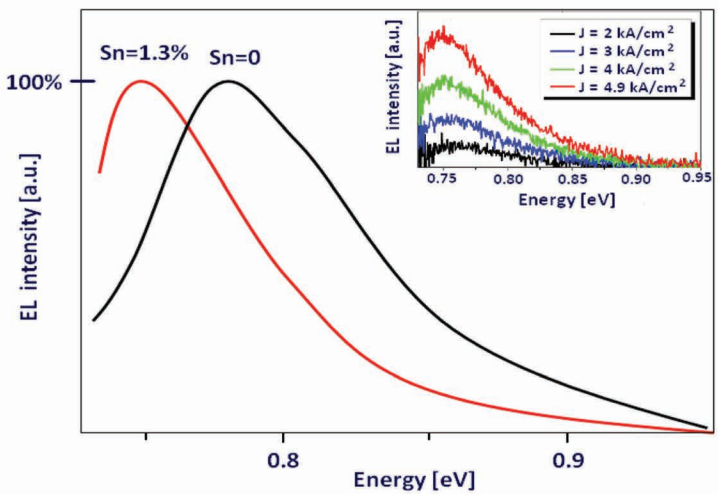

Figure 11.10 Electroluminescence from Ge and GeSn p-i-n junctions on Ge VS (J = 4.9 kA/cm^2). Inset shows current density dependence.

11.1.4 Material Science Challenges

GeSn has been identified as a material of interest for decades [5] for mainly three reasons: (i) the smaller bandgap than Ge extends the infrared range, (ii) a zero bandgap semiconductor may be created with around 40% Sn, and (iii) a direct bandgap transition (the only unstrained group IV direct semiconductor) may be obtained with a rather low Sn amount (8% Sn: expected crossover).

Progress was slow in the past because of serious material science challenges. Only recently, advanced epitaxy methods have pushed the growth of material good enough for device fabrication. The main material challenges stem from:

- Coexistence of a metallic phase and a semiconducting phase (α-Sn) around room temperature. Equilibrium phase transition of the semiconductor/metal takes place at 13°C.
- Large lattice mismatch between α-Sn and Ge (14.7%).
- Large GeSn alloy mixing gap with two-phase equilibrium already there when the Sn amount is more than 1%.
- Low growth temperatures as Sn melts at above 230°C.

Some research groups [21] have overcome the lattice mismatch problem with ternary group III–V compound substrates (Fig. 11.11). The group III–V compounds like GaInAs and GaInSb span the full range of lattice constants for GeSn.

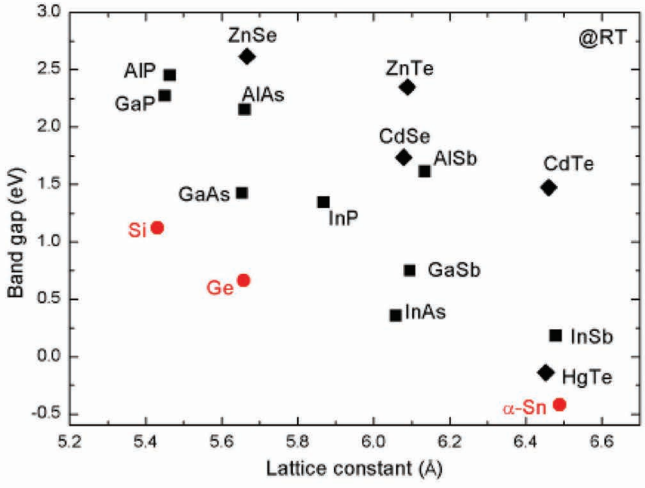

Figure 11.11 Bandgap versus lattice constant of group IV elements and group III–V and group II–VI compounds.

For Si photonics, the low-Sn-content GeSn alloy is addressed with acceptable lattice mismatch values if a VS is used. Even at low Sn amounts, equilibrium growth is not possible, as the phase diagram (Fig. 11.12) shows [5].

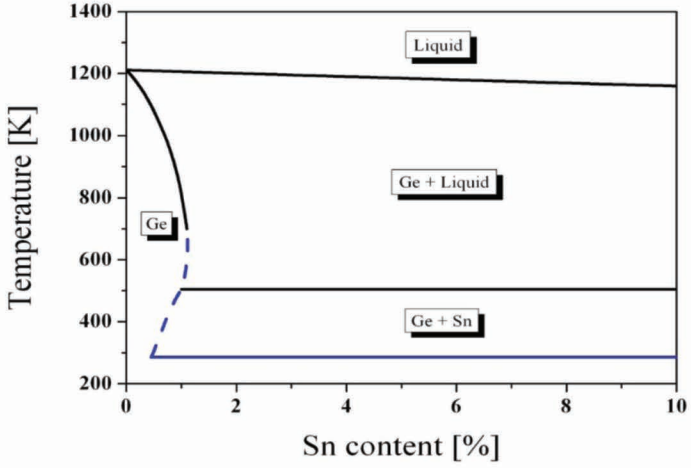

Figure 11.12 Phase diagram of the GeSn material system.

Look, for instance, at 5% Sn content. Then up to 500 K (around 230°C), the GeSn separates into a solid state mixture of Ge and Sn (Ge and Sn are doped to less than 1% by their counterparts); from 230°C to around 900°C, the mixture is solid Ge and liquid Sn droplets; and above 900°C both melt into a GeSn liquid. Modern epitaxy techniques like molecular beam epitaxy and chemical vapor deposition with specific precursors have allowed the epitaxial growth of single-phase GeSn on Si and Ge VS substrates at temperatures low enough (100°C–350°C) to overcome the equilibrium splitting into two phases. Generally, a nonequilibrium supersaturation of point defects (vacancies, interstitials) may occur at these low growth temperatures. Often, annealing steps are introduced during growth to reduce point defect levels and to improve dislocation structure.

11.1.5 Ternary Silicon Germanium Tin Alloys

A wider space in the lattice constant and band offsets may be obtained with ternary alloys. The ternary alloy SiGeSn may gain

importance for lattice-matched quantum well structures and mid-infrared (0.2–0.6 eV) devices. An overview about calculation of the bandgaps and their photonic applications is given in Ref. [3]. The lattice constant a of the ternary alloy $Si_x\,Ge_{1-x-y}\,Sn_y$ is given by

$$a = a_{Si} \cdot x + a_{Ge}(1 - x - y) + a_{Sn} \cdot y + b'_{SiGe}\, x(1 - x) b'_{SnGe} y(1 - y), \tag{11.6}$$

The lattice constants of Si, Ge, and Sn were taken as 0.54307 nm, 0.56575 nm, and 0.64912 nm, respectively. The lattice bowing parameters b' were chosen as $b'_{SiGe} = -0.026$ and $b'_{GeSn} = -0.166$, while the bowing of SiSn was taken as zero.

The most interesting applications of ternary alloys concern the possibility of creating lattice-matched quantum wells with practically usable band offsets. In Fig. 11.13 the direct conduction band energy (Γ) and the valence band edge E_v are shown as functions of the Sn content for a lattice-matched GeSiSn/GeSn heterojunction [25].

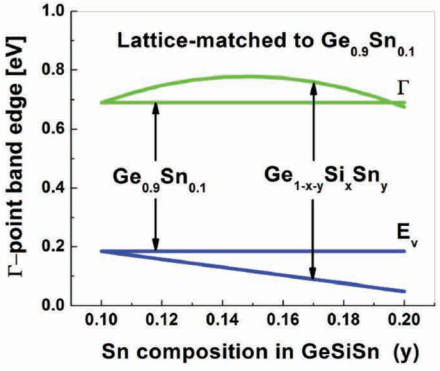

Figure 11.13 Direct conduction band edge and valence band edge of a lattice-matched Ge SiSn/$Ge_{0.9}Sn_{0.1}$ heterojunction [25].

As seen in Fig. 11.13 the ternary alloy may be used as a barrier material with around 100 meV energy barrier to the GeSn well.

11.2 Tensile-Strained Germanium

Generally, strain shifts the energies of the valence edges and band and the conduction band may split into sub-bands from otherwise

degenerate states. Such degenerate states are light and heavy holes (lh and hh) or the fourfold degenerate indirect L valleys in the conduction band. We consider now the biaxial stress of a GeSn layer on a (001) substrate. Biaxial stress leads to a tetragonal distortion of the strained lattice cell with equal strain ε in the in-plane directions (x and y) and an opposite perpendicular strain $\varepsilon_{\text{perp}}$ (z direction).

$$\varepsilon_{\text{perp}} = -\varepsilon \frac{2\upsilon}{1-\upsilon} \tag{11.7}$$

Here v is the Poisson ratio, which is assumed to be equal to $v = 0.27$.

Tetragonal distortion of the lattice cell may be considered as a sum of volume change ($2\varepsilon + \varepsilon_{\text{perp}}$) by all-around compression and a uniaxial extension in the perpendicular direction ($\varepsilon_{\text{perp}} - \varepsilon$). This two-term representation of biaxial stress is performed because all fundamental measurements of strained materials are done by volume change in a high-pressure cell and by uniaxial dilatation of a material rod. The volume change of a biaxial stressed epitaxial layer is given by (the numbers are calculated with $\upsilon = 0.27$)

$$2\varepsilon + \varepsilon_{\text{perp}} = 2\left(\frac{1-2\upsilon}{1-\upsilon}\right)\varepsilon = 1.26\varepsilon \tag{11.8}$$

and the uniaxial strain along the z direction is given by

$$\varepsilon_{\text{perp}} - \varepsilon = -\frac{1-\upsilon}{1+\upsilon}\varepsilon = -1.74\varepsilon. \tag{11.9}$$

The hydrostatic strain component (Eq. 11.8) causes an energy shift of the valence and conduction bands; the difference between both is measured as a bandgap change. For an overview on general strain effects, see Ref. [21]. The change in the bandgap energy is proportional to the hydrostatic deformation potential parameter a_g. The direct transition deformation potential values for the coefficient $a_g(\Gamma)$ vary around –10 eV (+/– 20%), as discussed in more detail in Ref. [26]. The coefficients $a_g(\text{L})$ for the indirect transition are also negative but much smaller (about –2.5 eV), with a relative uncertainty of more than 20%.

The large variations in deformation potential values result in uncertainties regarding bandgap extraction from strained materials. In the future biaxial stressed epitaxy layers may be used as a test material for the refinement of deformation potential measurements, but it is crucial to use well-defined structure parameters.

The uniaxial component (Eq. 11.9) causes a splitting of the valence band edge for the hh and lh bands. There is no splitting in the conduction band because the *L* valleys in the <111> direction are symmetric to the substrate orientation. This is simpler than in the SiGe/Si case, where the dominating indirect *X* valleys are split in the in-plane and perpendicular conduction sub-bands. The uniaxial deformation potential value b_g for the (100) substrate orientation amounts to about −2.5 eV. The deformation potential value b_g is the same for direct and indirect bands in the given orientation because both transitions address the same valence sub-bands, lh or hh.

The relation between strain and the lh bandgap is slightly nonlinear. The reason is given by the interaction with the third valence sub-band (spin-orbit split-off band), which is not considered here because its energy levels are lower by the split orbit energy difference $\Delta_0 = 0.287$ eV. Combining Eqs. 11.8 and 11.9, we obtain for biaxially stressed Ge the linear relations for the direct transitions to the lh and hh valence sub-bands. These linear relations may be used up to 1% strain; for higher values the nonlinear interaction with the split-off valence band has to be taken into account [26].

$$E_g(\text{lh}) = E_g(0) + \varepsilon(1.26a + 1.74b) \tag{11.10}$$

$$E_g(\text{hh}) = E_g(0) + \varepsilon(1.26a - 1.74b) \tag{11.11}$$

For compressive strain (negative value of ε), the hh bandgap is the lower one (Eq. 11.11) and this will dominate the bandgap emissions. The direct transition (hh) is clearly above the unstrained energy value $E_g(0)$ because the large deformation potential parameter *a* dominates. For indirect transition (hh) the energy is roughly strain independent because the smaller *a* coefficient contribution is partly cancelled by the *b* term. The compressive biaxial stress enhances the indirect character of Ge; it is only interesting for adjusting the modulation wavelengths of electroabsorption modulators.

The most important stress situation in Si-based photonics is given by tensile biaxial stress (Eq. 11.10). The energy of the direct transition decreases faster than that of the indirect transition, yielding a crossover between indirect/direct conduction bands at about 2% in-plane strain. The band energy decreases to about 0.5 eV at 2% in-plane strain, resulting in a 2.5 μm emission wavelength for the crossover situation. The crossover with uniaxial stress needs much higher strain levels (about 5%).

11.3 Conclusions

Application of strain and alloying of Ge with Sn are the prime candidates for the extension of the wavelengths in Si-based photonics beyond 1.6 μm toward the midinfrared regime. Biaxial in-plane stress leads to a tetragonal distortion of the lattice cell. Tensile strain favors reduction of the energy separation between direct band and indirect band (136 meV in unstrained Ge), and it reduces the bandgap to 0.5 eV for 2% biaxial tensile strain. For this biaxial strain value, an indirect-direct crossover takes place in the semiconductor. Uniaxial strain is less effective, requiring 5% for the conduction band crossover.

GeSn is a promising small-bandgap group IV semiconductor. Infrared shift of absorption, direct luminescence, and reflection are proven experimentally (extended infrared window for silicon-based photonics). First fundamental devices (photodetector, LED, optically stimulated lasers) are demonstrated with infrared light emission and detection up to 3 μm wavelength. Direct-indirect crossover takes place for strain-relaxed GeSn with about 7%–9% Sn amount. The crossover GeSn shows a similar bandgap reduction (to 0.5 eV) as the strained Ge.

Advanced metastable material preparation paved ways to direct group IV semiconductors for midinfrared (>2.5 μm) silicon-based photonics. The groups of John Kouvetakis and Jose Menendez [24] demonstrated the growth of GeSn layers with high Sn contents (13%–27%) directly on Si. The high lattice mismatch of GeSn on Si forced a rapid mismatch accommodation at the interface, resulting in layers with a rather small residual strain (between –0.5% and +0.2%). The cut-off wavelengths of these layers shifted from 3 μm to 8 μm with increasing Sn content.

Material science and fabrication fights with nonequilibrium alloy formation, lattice mismatch accommodation, strain management, defect creation from dislocation networks, and ultralow temperature processing, but steep progress is expected.

References

1. X. Sun, J. Liu, L. C. Kimerling and J. Michel (2009). Room-temperature direct bandgap electroluminesence from Ge-on-Si light-emitting diodes, *Opt. Lett.*, **34**, 1198.
2. E. Kasper, M. Oehme, J. Werner, T. Aguirov and M. Kittler (2012). Direct band gap luminescence from Ge on Si pin diodes, *Front. Optoelectron.*, **5**, 256.
3. P. Moontragoon, R. A. Soref and Z. Ikonic (2012). The direct and indirect bandgaps of unstrained $Si_xGe_{1-x-y}Sn_y$ and their photonic device applications, *J. Appl. Phys.*, **112**, 073106.
4. P. Boucaud, M. El Kurdi and J. M. Hartmann (2004). Photoluminescence of a tensilely strained silicon quantum well on a relaxed SiGe buffer layer, *Appl. Phys. Lett.*, **85**, 46.
5. E. Kasper, J. Werner, M. Oehme, S. Escoubas, N. Burle and J. Schulze (2012). Growth of silicon based germanium tin alloys, *Thin Solid Films*, **520**, 3195.
6. E. Kasper, N. Burle, S. Escoubas, J. Werner, M. Oehme and K. Lyutovic (2012). Strain relaxation of metastable SiGe/Si: investigation with two complementary X-ray techniques, *J. Appl. Phys.*, **111**, 063507.
7. V. R. D'Costa, C. S. Cook, A. G. Birdwell, C. L. Littler, M. Canonico, S. Zollner, J. Kouvetakis and J. Menendez (2006). Optical critical points of thin-film $Ge_{1-y}Sn_y$ alloys: a comparative $Ge_{1-y}Sn_y/Ge_{1-x}Si_x$ study, *Phys. Rev. B*, **73**, 125207.
8. S. Alberi, J. Blacksberg, L. D. Bell, S. Nikzad, K. M. Yu, O. D. Dubon and W. Walukiewicz (2008). Band anticrossing in highly mismatched Sn_xGe_{1-x} semiconducting alloys, *Phys. Rev. B*, **77**, 073202.
9. L. Vegard (1921). Die Konstitution der Mischkristalle und die Raumfüllung der Atome, *Z. Phys.* (in German) **5**, 17–26.
10. R. S. Bauer and G. Margaritondo (1987). Probing semiconductor/semiconductor interfaces, *Phys. Today*, **40**, 27.
11. G. Sun, R. A. Soref and H. H. Cheng (2010). Design of a Si-based lattice-matched room-temperature GeSn/GeSiSn multi-quantum-well mid-infrared laser diode, *Opt. Express*, **18**, 19957.
12. M. Oehme, M. Schmid, M. Kaschel, M. Gollhofer, D. Widmann, E. Kasper and J. Schulze (2012). GeSn p-i-n detectors integrated on Si with up to 4% Sn, *Appl. Phys. Lett.*, **101**, 141110.
13. J. Mathews, R. Roucka, J. Xie, S.-Q. Yu, J. Menendez and J. Kouvetakis (2009). Extended performance GeSn/Si(100) p-i-n photodetectors for

full spectral range telecommunication applications, *Appl. Phys. Lett.*, **95**, 133506.

14. S. Su, B. Cheng, C. Xue, W. Wang, Q. Cao, H. Xue W. Hu, G. Zhang, Y. Zuo and Q. Wang (2011). GeSn p-i-n photodetector for all telecommunication bands detection, *Opt. Express*, **19**, 6400.
15. J. Werner, M. Oehme, M. Schmid, M. Kaschel, A. Schirmer, E. Kasper and J. Schulze (2011). Germanium-tin p-i-n photodetectors integrated on silicon grown by molecular beam epitaxy, *Appl. Phys. Lett.*, **98**, 061108.
16. R. Roucka, J. Mathews, R. Beeler, J. Tolle, J. Kouvetakis and J. Menendez (2011). Direct gap electroluminescence from Si/Ge1−ySny p-i-n heterostructure diodes, *Appl. Phys. Lett.*, **98**, 061109.
17. J. Matthews, R. Roucka, J. Xie, S.-Q. Yu, J. Menendez and J. Kouvetakis (2009). Extended performance GeSn/Si(100) p-i-n photodetectors for full spectral range telecommunication applications, *Appl. Phys. Lett.*, **95**, 133506.
18. M. Oehme, J. Werner, M. Gollhofer, M. Schmid, M. Kaschel, E. Kasper and J. Schulze (2011). Room-temperature electroluminescence from GeSn light-emitting pin diodes on Si, *IEEE Photonics Technol. Lett.*, **23**, 1751–1753.
19. M. Oehme, E. Kasper and J. Schulze (2012). GeSn photodetection and electroluminescence devices on Si, *ECS Trans.*, **50**(9), 583–590.
20. T. Arguirov (2014). Pers. Communication.
21. H. Lin, R. Chen, W. Lu, Y. Huo, T. I. Kamins and J. S. Harris (2012). Investigation of the direct band gaps in $Ge_{1-x}Sn_x$ alloys with strain control by photoreflectance spectroscopy, *Appl. Phys. Lett.*, **100**, 102109.
22. S.-Q. Liu and S.-T. Yen (2019). Extraction of eight-band k · p parameters from empirical pseudopotentials for GeSn, *J. Appl. Phys.*, **125**, 245701.
23. H. Tran, W. Du, S. A. Ghetmiri, A. Mosleh, G. Sun, R. A. Soref, J. Margetis, J. Tolle, B. Li, H. A. Naseem and S.-Q. Yu (2016). Systematic study of $Ge_{1-x}Sn_x$ absorption coefficient and refractive index for the device applications of Si-based optoelectronics, *J. Appl. Phys.*, **119**, 103106.
24. C. Xu, P. M. Wallace, D. A. Ringwala, S. L. Y. Chang, C. D. Poweleit, J. Kouvetakis and J. Menéndez (2019). Mid-infrared (3-8 μm) $Ge_{1-y}Sn_y$ alloys ($0.15 < y < 0.30$): synthesis, structural, and optical properties, *Appl. Phys. Lett.*, **114**, 212104.
25. G. Sun (2011). ICSI-7, Invited Talk.
26. E. Kasper and M. Oehme (2015). Germanium tin light emitters on silicon, *Jpn. J. Appl. Phys.*, **54**, 04DG11.